Journal of Nanobiotechnology

RESEARCH

Open Access

Hypoxia-responsive core-cross-linked supramolecular nanoprodrug based on dendritic drug-drug conjugates for synergetic anticancer therapy

Yue Ding[1*], Yu Xie[1], Liangshun Zheng[1], Mingguang Lin[3], Yihai Shi[4], Tingting Chen[1], Chang Du[2*], Jin Ding[2*] and Beifang Ning[3*]

Abstract

Background Recently, the strategy of self-assembling dendritic drug-drug conjugates into supramolecular nanoprodrug was widely explored in biomedical applications. Herein, we construct a hypoxia-responsive core-cross-linked supramolecular nanoprodrug (CSN-IR806/CB) based on a dendritic drug-drug conjugate.

Methods We prepared a hypoxia-responsive dendritic drug-drug conjugates IR806-(Azo-CB)$_4$, which was combined with β-cyclodextrin-pendant poly(ethylene glycol)-block-poly(glutamic acid) block copolymer (PEG-PGlu-CD) to construct the core-cross-linked supramolecular nanoprodrug (CSN-IR806/CB) with enhanced physiological stability through the synergy of π-π stacking interaction, host-guest complexation, hydrogen bonds, and hydrophobic interaction.

Results The near-infrared (NIR) light irradiation of the CSN-IR806/CB treated tumor cells induced IR806-mediated PDT and PTT, and aggravated hypoxia, which triggered the disassembly of CSN-IR806/CB and the subsequent release of activated CB for synergetic cancer cell killing.

Conclusions The CSN-IR806/CB can realize a synergistic triple therapeutic effect of photothermal therapy (PTT), photodynamic therapy (PDT), and chemotherapy (CT; i.e., PTT-PDT-CT).

Keywords Hypoxia, Host-guest complexation, Dendritic drug-drug conjugate, Supramolecular nanoprodrug, Combination therapy

*Correspondence:
Yue Ding
yueding@ntu.edu.cn
Chang Du
duchang19901030@163.com
Jin Ding
dingjin1103@163.com
Beifang Ning
ningbeifang@163.com

[1]School of Chemistry and Chemical Engineering, Nantong University, Nantong 226019, P. R. China
[2]Clinical Cancer Institute, Center for Translational Medicine, Naval Medical University, Shanghai, China
[3]Department of Gastroenterology, Changzheng Hospital, Naval Medical University, Shanghai, China
[4]Department of Gastroenterology, Shanghai Pudong New Area Gongli Hospital, Shanghai 200135, China

Background

Nanomedicine-based drug delivery systems (DDSs), which possess some advantages of simultaneous delivering multiple drugs, enhancing drug solubility, and prolonging blood circulation, can effectively deliver anticancer drugs to tumor site via the enhanced permeation and retention (EPR) effect, and then specifically release anticancer drugs in tumor site [1–5]. Among them, nanoprodrug has received increasing attention owing to higher drug-loading efficiency and lower potential systematic toxicity, which is established through various conjugation approaches such as polymer-drug conjugates and drug-drug conjugates [6–9]. The drug-drug conjugates are always synthesized by coupling two or more types of drug molecules through stimuli-responsive linkages, which can be disintegrated under corresponding stimulus to release activated drugs [10–12].

Especially, dendrimer is emerging as promising drug-drug conjugates on account of its unique dendritic structure and multivalent cooperativity, resulting from its highly branched yet precisely controllable architecture [13, 14]. However, the dendritic drug-drug conjugates still present certain obstacles for constructing nanoprodrug, such as complex synthesis process, uncontrolled drug release behaviors, and the limited selection of anticancer drugs [15]. In light of this, the introduction of macrocyclic molecules with a cavity may provide an available strategy for improving the above issues by encapsulating the dendrimer-based drug-drug conjugate via host-guest complexation [16–19]. Against this background, supramolecular dendritic drug-drug conjugates show great potential for the development of desired nanomedicine.

Inspired by the key characteristic of hypoxia in numerous solid tumors, which is caused by rapid cell proliferation and insufficient neovasculature, a series of bio-reductive prodrugs containing hypoxia-responsive linkers have been employed in hypoxic imaging and therapy [20–24]. Azobenzene (AZO) linker is the most widely used function group in the design of hypoxia-responsive DDSs, which can be reduced to aniline group in the presence of nicotinamide adenine dinucleotide phosphate (NADPH) and azo reductase under hypoxic tumor microenvironment [25–28]. In addition, photodynamic therapy (PDT) is generally combined with the hypoxia-responsive DDSs for that PDT can aggravate the underlying hypoxia by employing photosensitizers to facilitate the conversion of oxygen into cytotoxic reactive oxygen species (ROS) under light irradiation [29–31].

Herein, we rationally designed a hypoxia-responsive dendritic drug-drug conjugates IR806-(Azo-CB)$_4$, which was synthesized by appending chlorambucil (CB) to the terminals of IR806-containing dendritic structure via azobenzene linkages with the aim of achieving hypoxia-responsive drug release under hypoxic conditions. Subsequently, IR806-(Azo-CB)$_4$ self-assembled into core-cross-linked supramolecular nanoprodrug CSN-IR806/CB combined with β-cyclodextrin grafted PEG-block-poly(glutamic acid) block copolymer (PEG-PGlu-CD) via the synergy of π-π stacking interaction, host-guest complexation, hydrogen bonds, and hydrophobic interaction (Scheme 1). Outstandingly, the host-guest complexation between β-cyclodextrin and chlorambucil (CB) endowed CSN-IR806/CB with a cross-linked core, which greatly enhanced the stability of this supramolecular nanoprodrug. After internalization of CSN-IR806/CB into HepG2 cells, IR806 mediated photothermal therapy (PTT) and PDT under near-infrared (NIR) light irradiation. Due to the consumption of oxygen, the creating PDT-enhanced hypoxic environment accelerated the release of activated CB through the cleavage of AZO linkers. Therefore, we have successfully fabricated a hypoxia-responsive core-cross-linked supramolecular nanoprodrug CSN-IR806/CB to achieve a synergistic triple therapeutic effect of PTT, PDT, and chemotherapy (CT; i.e., PTT-PDT-CT).

Materials and methods

Synthesis of Boc-D2-(Azo-CB)$_4$

The Azo-CB-COOH (456.3 mg, 1.25 mmol) and (7-Azabenzotriazol-1-yl)-N, N,N',N'-tetramethyluronium hexafluorophosphate (HATU) (760 mg, 2 mmol) were dissolved in 10 mL of anhydrous DMF and stirred at 0 °C for 5 h. Following this, DIPEA (348 mg, 2.7 mmol) introduced into the mixture, which was then allowed to warm up to room temperature. Solution of Boc-D2 (105.6 mg, 0.125 mmol) in 5 mL dry DMF was added gradually while stirring continued for an additional forty-eight hours. The reaction was terminated by adding water and subsequently extracted with dichloromethane (DCM). The organic phase was dried using sodium sulfate before removing the solvent under reduced pressure. Finally, the crude product underwent purification through column chromatography on silica gel yielding an orange-red solid Boc-D2-(Azo-CB)$_4$ (128.3 mg. 46.2% yield).

Synthesis of IR806-(Azo-CB)$_4$

Initially, trifluoroacetic acid (TFA) (1 mL) was added slowly to solution of Boc-D2-(Azo-CB)$_4$ (130 mg, 0.058 mmol) in 1 mL DCM and stirred for 2 h. The solvent along with any unreacted TFA was then evaporated under reduced pressure, resulting in an orange-red solid of D2-(Azo-CB)$_4$ after vacuum drying. Next, IR806 (80 mg, 0.1 mmol) and HATU (58 mg, 0.15 mmol) were dissolved in 5 mL dry DMF and stirred for 3 h at 0 ℃. DIPEA (0.5 mL, 0.003 mmol) was introduced into the mixture which was then allowed to warm up to room temperature. A solution of D2-(Azo-CB)$_4$ (217.5 mg, 0.097 mmol) in 2 mL dry DMF was added dropwise into the front solution while stirring continued for another 24 h. The resulting

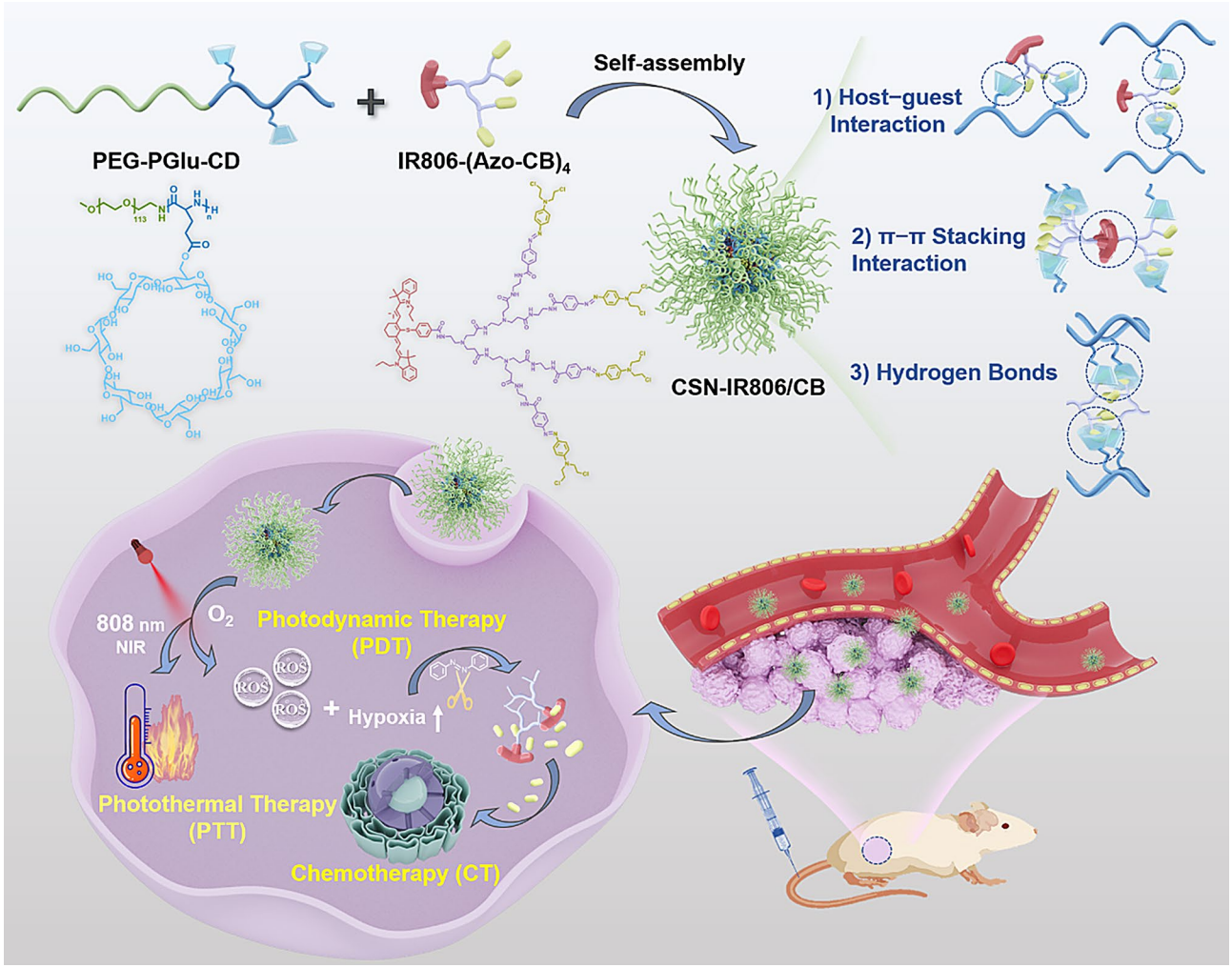

Scheme 1. Schematic illustration for the fabrication of hypoxia-responsive core-cross-linked supramolecular nanoprodrug CSN-IR806/CB and the mechanism of PTT-PDT-CT

solution was placed into a dialysis tube (MWCO 2000 Da), dialyzed against DMSO for twenty-four hours followed by ultrapure water for an additional twenty-four hours before being freeze-dried to yield IR806-$(Azo\text{-}CB)_4$ (242.67 mg, 86.3% yield).

Synthesis of PEG-PBGlu

$PEG\text{-}NH_2$ (187 mg, 0.037 mmol) was used as the initiator and added to a solution of Bn-Glu-NCA (300 mg, 1.28 mmol) in 4 mL of dry DMF while stirring continuously at room temperature for 48 h under a nitrogen atmosphere. The reaction mixture was then precipitated by adding diethyl ether (20 mL) to collect the white precipitate via centrifugation. This precipitate was dried overnight in a vacuum oven to yield PEG-PBGlu (196.6 mg, 86.4%).

Synthesis of PEG-PGlu-CD

PEG-PBGlu (100 mg, 0.074 mmol) was dissolved in 20 mL of a 1 M sodium hydroxide solution and stirred vigorously while refluxing at 100 °C overnight. The resulting reaction mixture was then placed into dialysis tubing and dialyzed against deionized water for 48 h to eliminate sodium hydroxide and dissociated protective groups, yielding PEG-PGlu (70.4 mg, 85% yield).

Subsequently, PEG-PGlu (50 mg, 0.0074 mmol), EDC (12 mg, 0.077 mmol), DMAP (5 mg, 0.04 mmol), and β-Cyclodextrin (106.3 mg, 0.094 mmol) were dissolved in 5 mL dry DMF. The mixture was then stirred for an additional twenty-four hours at room temperature. Finally, the reaction mixture was precipitated by adding diethyl ether (20 mL) to collect the white solid sediment of PEG-PGlu-CD (91.96 mg, 35.3% yield).

Fabrication of core-cross-linked supramolecular nanoprodrug CSN-IR806/CB

Typically, PEG-PGlu-CD (4 mg) and IR806-$(Azo\text{-}CB)_4$ (2 mg) was dissolved in 1 mL of DMF. Subsequently, 5 mL of PBS was added to the solution while stirring vigorously

overnight. The resulting mixture was then placed into a dialysis tube (MWCO 3500 Da) and dialyzed against PBS to yield CSN-IR806/CB.

Detection of $^1O_2$ generation

ABDA (0.05 mg/mL) was introduced into 20 mL of PBS containing CSN-IR806/CB. To trigger the release of $^1O_2$ using NIR, this solution was exposed to NIR irradiation at 808 nm with an intensity of 1.0 W/cm² for 5 min. Due to ABDA's ability to effectively capture ROS through a rapid reaction with its anthracene moiety, the initial UV-Vis absorption of ABDA would gradually decrease in the presence of $^1O_2$.

In vitro drug release

A solution of CSN-IR806/CB (1 mg/mL) was mixed with varying concentrations of $Na_2S_2O_4$ at 1.6, 3.2, 6.4, 12.8, or 25.6 mM. After stirring the mixture for 2 h, it was placed in a dialysis bag (MWCO: 500 Da) and immersed in methanol (15 mL) while stirring for 24 h. The methanol solution outside the dialysis bag was then evaporated and analyzed using HPLC.

In vitro cytotoxicity

HepG2, HeLa, and MCF-7 cells were seeded in a 96-well plate at a density of 1×10^4 cells per well (200 μL) and incubated in DMEM for 12 h. After this period, the medium was replaced with fresh DMEM containing varying concentrations of CSN-IR806/CB and incubated for an additional 6 h under either hypoxic or normoxic conditions. For the irradiation groups, the cells received NIR exposure (808 nm, 1.0 W/cm², for 5 min), followed by another incubation period of 18 h. The cytotoxicity was then assessed using MTT assays. In addition, live/dead staining was performed on HepG2 cells using fluorescein diacetate and propidium iodide before imaging them with a fluorescent microscope.

Cell internalization

HepG2 cells were plated in a 12-well plate at a density of 1.0×10^5 cells per well and incubated in DMEM for 12 h. Following this, the medium was replaced with fresh DMEM containing either CSN-IR806/CB or free IR806 at a concentration of 4 μg/mL. After incubation for either 1–4 h under hypoxic or normoxic conditions, the cells were stained with DAPI for 20 min and then observed using a confocal laser scanning microscope (CLSM).

Intracellular ROS generation

HepG2 cells were plated in a 12-well plate at a density of 1.0×10^5 cells per well and incubated in DMEM for 12 h. Subsequently, the medium was replaced with fresh DMEM containing CSN-IR806/CB at an IR806 concentration of 4 μg/mL. After a 4 h incubation period, the irradiation groups received NIR exposure (808 nm, 1.0 W/cm², for 5 minutes). Following this, the cells were stained with 2, 7-dichlorodihydrofluorescein diacetate (DCFH-DA) for 20 min and examined using a fluorescence microscope.

In vivo biodistribution

The experimental protocol was approved by the Nantong University Institutional Animal Care and Use Committee. Nude mice with HepG2 tumors (approximately 80 mm³) were randomly assigned to three groups ($n = 3$) and treated intravenously with either free IR806, free CB, or CSN-IR806/CB, using a dose of 5 mg/kg for CB or 4.2 mg/kg for IR806. At specified time points, in vivo tumor accumulation and biodistribution were assessed using a Kodak multimode imaging system. Major organs and tumors were collected at 12 h and 24 h post-injection for ex vivo distribution imaging. The amount of IR806 was extracted and quantified through fluorescence spectroscopy.

In vivo antitumor activity

Nude mice bearing HepG2 tumors (60–70 mm³) were randomly assigned to five groups ($n = 4$) and treated intravenously with PBS, free CB, free IR806 + L, CSN-IR806/CB, or CSN-IR806/CB + L at CB equivalent dose of 5 mg/kg and IR806 dose of 4.2 mg/kg on day 0 and day 5. Mice in the IR806 + L and CSN-IR806/CB + L groups underwent NIR irradiation (808 nm, 1.0 W/cm² for 5 min) 12 h after injection. Tumor size and body weight were monitored at designated time points. The tumor volume (V) was calculated according to equation: $V = 0.5 \times \text{Length} \times \text{Width}^2$, and the tumor inhibitory rates (TIR) was calculated by equation: TIR (%) = 100 × (mean V of PBS group - mean V of others)/(mean V of PBS group).

Statistical analysis

All data were provided as mean ± standard deviation (SD). The statistical significance of different groups was given by using Student's *t*-test.

Results and discussion

Synthesis and characterization of core-cross-linked supramolecular nanoprodrug CSN-IR806/CB

The hypoxia-responsive dendritic drug-drug conjugates IR806-$(Azo\text{-}CB)_4$ was successfully synthesized by appending the chlorambucil (CB) to the IR806-initial-modified dendrimer terminals via hypoxia-cleavable azobenzene linkages with the aim of achieving controllable drug release, and the PEG-PGlu-CD was prepared by grafting β-cyclodextrin onto poly(ethylene glycol)-block-poly(glutamic acid) via biodegradable ester bonds (Additional file 1: Fig. S1). The relevant nuclear magnetic resonance spectroscopy illustrated in Additional file 1:

Fig. S2-S5, was confirm the structure of IR806-(Azo-CB)$_4$ and PEG-PGlu-CD. Additionally, the appearance of characteristic absorption peaks of Azo-CB and IR806 in UV-vis spectrophotometry and fluorescence spectra were both further approved the successful synthesize of IR806-(Azo-CB)$_4$ (Fig. 1A-C).

Sequentially, IR806-(Azo-CB)$_4$ and PEG-PGlu-CD were self-assembled into core-cross-linked supramolecular nanoprodrug CSN-IR806/CB with ultrahigh stability via intra- and intermolecular noncovalent interactions, e.g. π-π stacking interaction, host-guest complexation, hydrogen bonds, and hydrophobic interaction [32, 33]. The PEG component functioned as the outer hydrophilic shell to enhance stability, inhibit non-specific adsorption, and prolong the blood circulation time [34]. While loading dendritic drug-drug conjugates IR806-(Azo-CB)$_4$, the formation of crosslinked core tremendously enhanced the stability of CSN-IR806/CB and avoided the premature leakage of drugs during the blood circulation. The coexistence of Azo-CB and IR806 in supramolecular nanoprodrug was confirmed by the characteristic absorption peaks at 273, 417, and 805 nm in UV-vis absorption spectra of CSN-IR806/CB (Fig. 1A). The drug loading efficiency of IR806 in CSN-IR806/CB was determined to be 10.6% according to the UV-vis absorbance, and then the drug loading efficiency of CB was calculated to be 12.7% according to the chemical structure of IR806-(Azo-CB)$_4$. Additionally, fluorescence spectra of TAPP and Azo-CB were detected inside CSN-IR806/CB. As shown in Fig. 1B, C, significant fluorescence of Azo-CB and IR806 were observed in CSN-IR806/CB upon excitation at 225 nm and 440 nm, respectively.

Subsequently, the size distribution and morphology of CSN-IR806/CB were investigated using dynamic light scattering (DLS), scanning electron microscope (SEM), and transmission electron microscopy (TEM) analyses. As shown in Fig. 1D-F, the hydrodynamic diameter (D_h) of CSN-IR806/CB was 205.3 ± 0.96 nm with a PDI of 0.145 ± 0.03, while the TEM and SEM image both exhibited uniform spherical morphology of CSN-IR806/CB with average diameter of 128.6 ± 6.3 nm and 135.8 ± 5.5 nm, respectively. Outstandingly, the core-shell structure of CSN-IR806/CB was clearly observed in the enlarged TEM image, which showed an outer PEG layer of about 10 nm and a cross-linked core with a diameter of approximate 92 nm (Fig. 1E). Furthermore, the biostability of SNP was assessed by measuring D_h in phosphate buffered saline (PBS) solution at 37 °C with 5%, 10%, or 15% fetal bovine serum (FBS) (Fig. 2A). The absence of significant changes in D_h within 24 h indicated the excellent biostability of CSN-IR806/CB under simulated physiological environments [35].

Photothermal and photodynamic properties

Considering the NIR photothermal responsiveness of IR806-based materials, the photothermal properties of CSN-IR806/CB was subsequently examined by monitoring temperature fluctuations in water solutions under

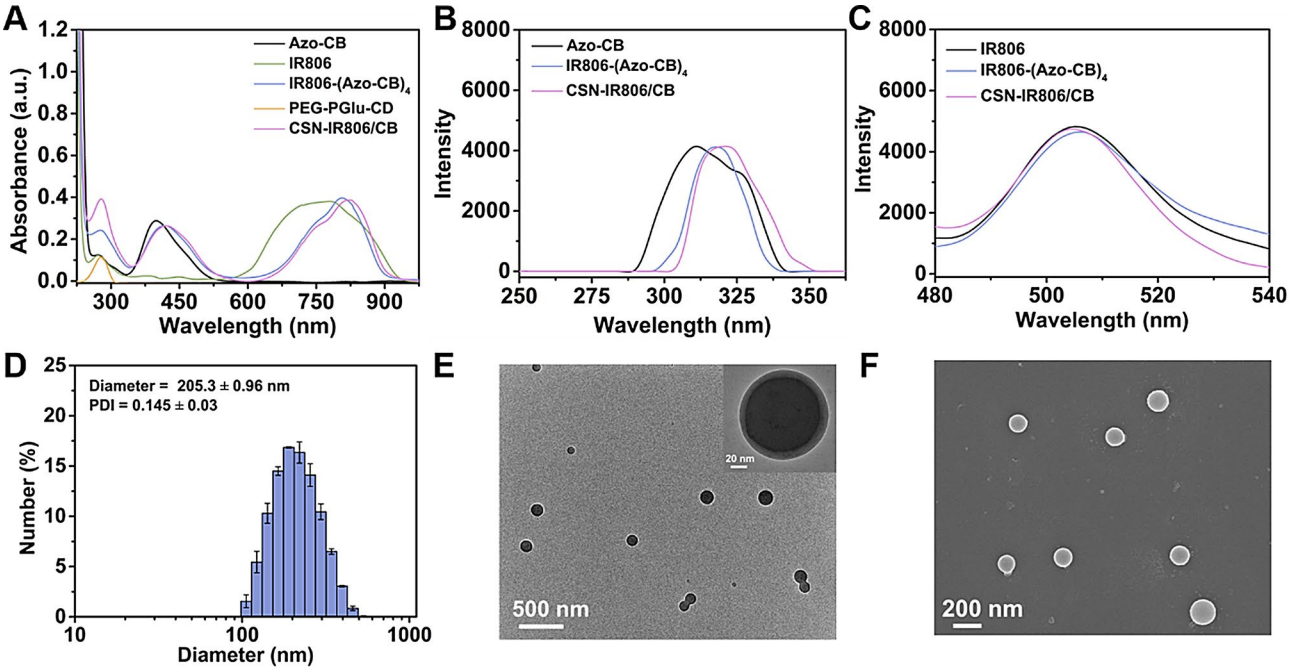

Fig. 1 (**A**) The UV-vis absorption spectra of Azo-CB, free IR806, IR806-(Azo-CB)$_4$, PEG-PGlu-CD, and CSN-IR806/CB. (**B**) Fluorescence spectra of Azo-CB, IR806-(Azo-CB)$_4$, and CSN-IR806/CB at the excitation wavelength of 225 nm. (**C**) Fluorescence spectra of free IR806, IR806-(Azo-CB)$_4$, and CSN-IR806/CB at the excitation wavelength of 440 nm. (**D**) DLS data, (**E**) TEM image and (**F**) SEM image of CSN-IR806/CB

808 nm NIR irradiation. As depicted in Fig. 2B, C, the maximum temperature increment (ΔT) of CSN-IR806/CB solutions (40 μg/mL IR806 equiv.) rapidly increased to 21.6 °C under NIR irradiation (808 nm, 1.0 W/cm^2, 5 min), which was obviously higher than that of the PBS control solution (3.8 °C) and free IR806 (14.6 °C) under the same NIR irradiation condition. In comparison to ΔT of free IR806, the ΔT increases of CSN-IR806/CB can be attributed to the enhanced π-π stacking interactions between IR806-(Azo-CB)$_4$ molecules within the supramolecular nanoprodrug CSN-IR806/CB, which can promote the energy relaxation [35]. Meanwhile, the photothermal effect of CSN-IR806/CB exhibited a dependence on both concentration and laser power intensity (Fig. 2D, E). Notably, PTT performance of CSN-IR806/CB remained stable after four cycles of repeated NIR irradiation (808 nm, 1.0 W/cm^2, 5 min), indicating excellent photostability (Fig. 2F). Based on the linear relationship between the cooling period of 808 nm laser off and ln (θ), the PTT conversion efficiency (η) of CSN-IR806/CB was calculated to be 33.4% (Additional file 1: Fig. S6) [36]. Consequently, the supramolecular nanoprodrug CSN-IR806/CB exhibit remarkable photothermal effect and photostability, making it highly suitable for in vitro and in vivo PTT.

Sequentially, the $^1O_2$ generation ability of CSN-IR806/CB under NIR irradiation was evaluated by using 9,10-anthracenediyl-bis(methylene) dimalonic acid (ABDA) as probe, which could specifically react with $^1O_2$ and then induce the decrease in its characteristic absorbance peaks [37]. Upon NIR irradiation (808 nm, 1.0 W/cm^2, 5 min) of the CSN-IR806/CB solution containing ABDA, the corresponding absorption intensities of ABDA at 397 nm decreased rapidly, indicating the efficient production of $^1O_2$ (Fig. 3A). By comparison, CSN-IR806/CB had the similar $^1O_2$ generation efficacy as free IR806, suggesting that the $^1O_2$ generation ability of photosensitizer IR806 was not affected by the conjugation with CB and loading in supramolecular nanoprodrug (Additional file 1: Fig. S7). Furthermore, the $^1O_2$ generation capability of CSN-IR806/CB under 808 nm NIR irradiation was estimated by electron spin resonance (ESR) spectroscopy using 2, 2, 6, 6-tetramethylpiperide (TEMP) as capture agent. As shown in Fig. 3B, we observed that the intensity of typical 1:1:1 ESR peaks gradually increased within 10 min under NIR irradiation ascribed to the characteristic triplet signal of TEMP/$^1O_2$ adduct (TEMPO), which was in accordance with the results of UV-vis absorbance [38]. Overall, these results validated the outstanding photodynamic property of CSN-IR806/CB.

Hypoxia-responsive drug release and property of CSN-IR806/CB

As for the reduction of an azobenzene linker to two aniline derivatives is tremendously influenced by the

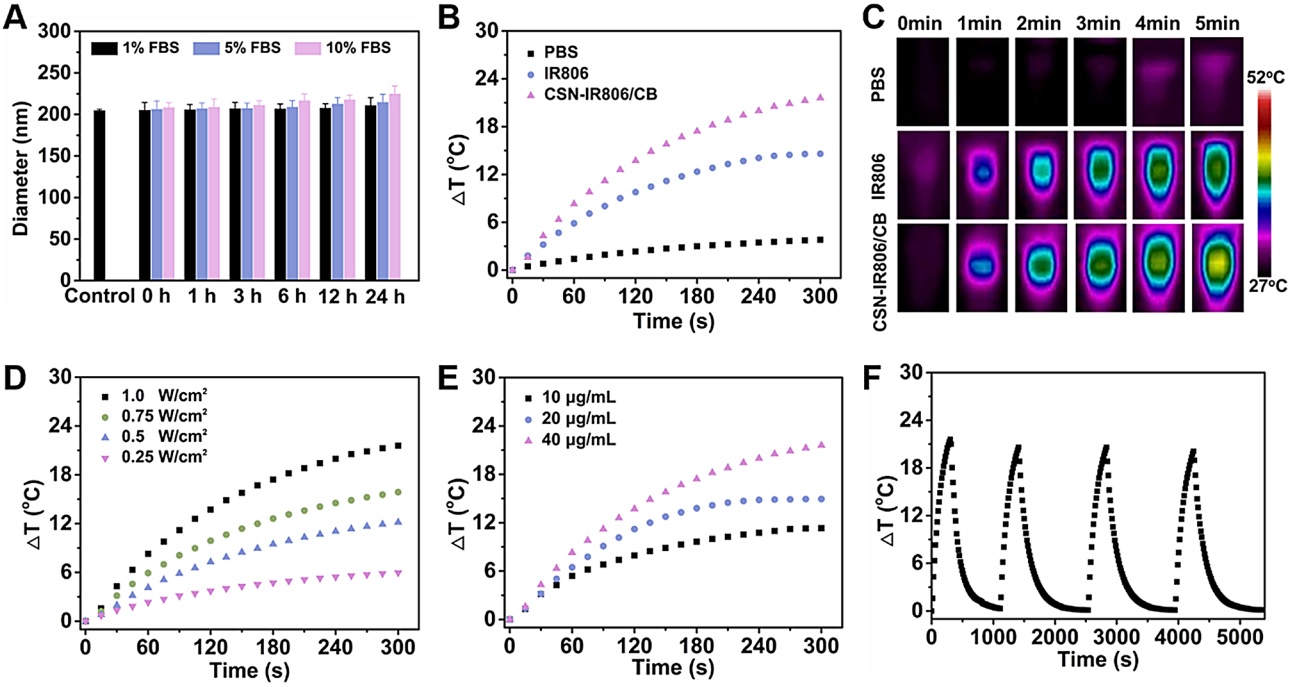

Fig. 2 (**A**) Hydrodynamic diameter distribution of CSN-IR806/CB incubated in different media for 24 h. (**B**) Photothermal heating effects and (**C**) infrared thermal images of PBS, free IR806, and CSN-IR806/CB solutions under 808 nm NIR irradiation (1.0 W/cm^2, 5 min). Photothermal heating effects of CSN-IR806/CB solution (**D**) under various power intensities or (**E**) with different concentrations. (**F**) Photothermal cycle curves of CSN-IR806/CB (40 μg/mL IR806 equiv.) under NIR irradiation (808 nm, 1.0 W/cm^2, 5 min) for four cycles

degree of hypoxia during this process, we monitored the hypoxia-responsive drug release by using high-performance liquid chromatography (HPLC) in the presence of sodium dithionite ($Na_2S_2O_4$) with different concentrations. Here, the $Na_2S_2O_4$ is generally applied to mimic different hypoxic condition for 2 h [39]. As illustrated in Fig. 3C, following the increase of $Na_2S_2O_4$ concentration, the peaks representing CB at 11.8 min gradually heightened. Simultaneously, the color of the CSN-IR806/CB solution was changed from green to yellow after the addition of $Na_2S_2O_4$ (Additional file 1: Fig. S8). These results indicated that the activated CB could be effectively released from CSN-IR806/CB under hypoxic condition. In addition, DLS and TEM were used to measure the corresponding size and morphological changes of CSN-IR806/CB incubated with $Na_2S_2O_4$ (25.6 mM) for 0.5 h, 1 h, and 2 h (Fig. 3D-G). The hydrodynamic diameter of CSN-IR806/CB distinctly became smaller and its initial spherical shape gradually disintegrated with time on account of the hypoxia-responsive disassembly.

In vitro cytotoxicity

The in vitro anticancer effect of CSN-IR806/CB against HepG2, HeLa, and MCF-7 cells was estimated through the 3-(4,5-dimethylthiazol-2-yl)-2,5-diphenyltetrazolium bromide (MTT) assay. Under normoxia without NIR irradiation, the cell viability decreased as the CB and IR806 concentration increased in CSN-IR806/CB and reached approximately 51.7% (HepG2), 48.8% (HeLa), and 53.2% (MCF-7) at a CB concentration and IR806 of 8 μg/mL and 6.68 μg/mL, respectively, indicating an inherent hypoxic environment within these cancer cells (Fig. 4A, S9A, and S10A). Whereas, the CSN-IR806/CB could effectively inhibit cell proliferation and enhance cell apoptosis with a half-maximal inhibitory concentration (IC_{50}) of 1.9 μg/mL (HepG2), 1.76 μg/mL (HeLa), and 2.03 μg/mL (MCF-7) after culturing in hypoxic condition without NIR irradiation, demonstrating that the hypoxia-triggered CB release from CSN-IR806/CB resulted in higher cytotoxicity. Otherwise, the CSN-IR806/CB exhibited the minimum IC_{50} of 0.71 μg/mL (HepG2), 0.69 μg/mL (HeLa), and 0.72 μg/mL (MCF-7), and the strongest cytotoxicity under hypoxia with NIR irradiation owing to the synergistic triple therapeutic effect of PTT-PDT-CT (Fig. 4B, S9B, and S10B). Despite the partial limitation of PDT efficacy under hypoxia, the decrease in oxygen levels induced a stronger chemotherapeutic effect by increasing CB release, which ultimately offset the weakening of PDT and resulted in minimum cell viability combined with the unaffected PTT effect.

To further validate the cytotoxicity of CSN-IR806/CB, calcein acetoxymethyl ester (calcein-AM) and propidium iodide (PI) were utilized for staining adherent HepG2 cells with green fluorescence indicating live cells and red fluorescence indicating dead cells. As shown in Fig. 4C, CSN-IR806/CB caused increased cell death (red color) when incubated under hypoxic conditions compared to normoxic conditions without NIR irradiation. Upon

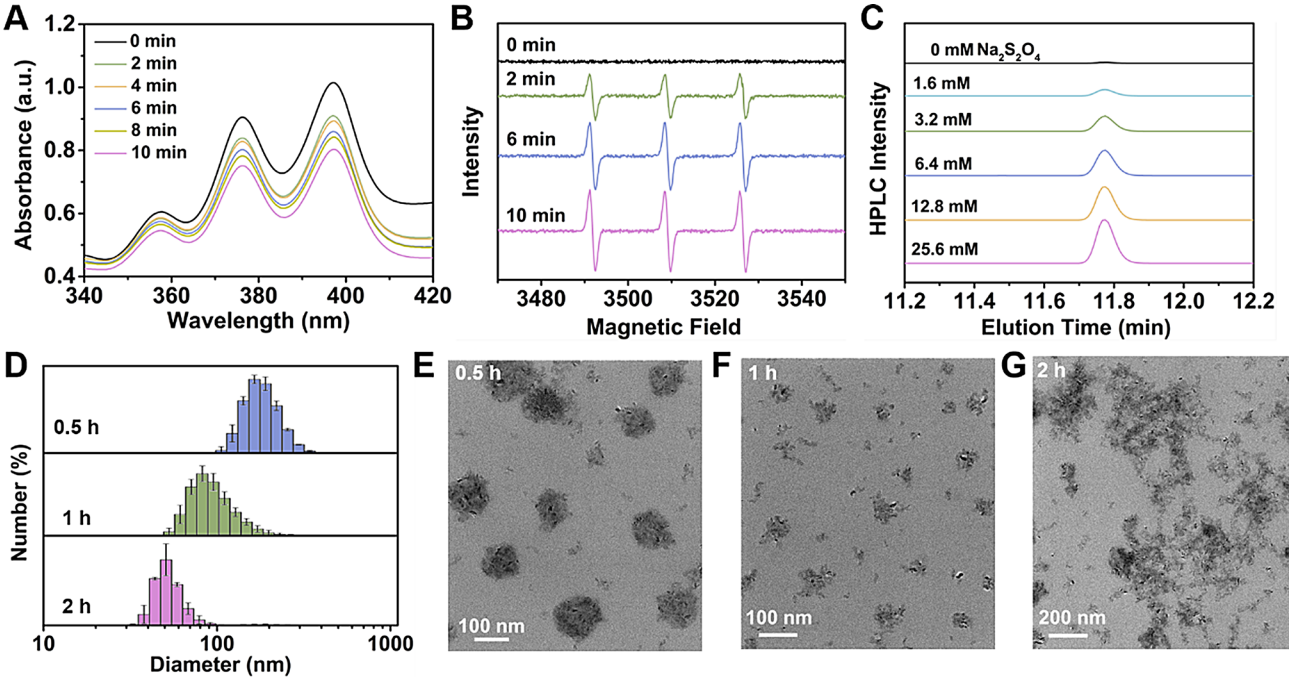

Fig. 3 (**A**) Absorption spectra of ABDA after NIR irradiation by $^1O_2$ generated from CSN-IR806/CB. (**B**) ESR analysis of $^1O_2$ production at the predetermined time points. (**C**) HPLC analysis of CB release triggered by different concentrations of $Na_2S_2O_4$. (**D**) Size changes of CSN-IR806/CB incubated with $Na_2S_2O_4$ of 25.6 mM. TEM images of CSN-IR806/CB incubated with $Na_2S_2O_4$ of 6.4 mM for (**E**) 0.5 h, (**F**) 2 h, and (**G**) 4 h

808 nm laser irradiation, much more cell death was displayed under hypoxia compared to that under normoxia, demonstrating the NIR irradiation could aggravate hypoxia to boost CD release and realize the synergistic triple therapeutic effect of PTT-PDT-CT.

In vitro ROS generation, cellular uptake, and ICD

To assess the intracellular ROS levels, HepG2 cells were incubated with CSN-IR806/CB under normoxic/hypoxic conditions with or without NIR irradiation, and the intracellular ROS levels were visualized by using 2,7-dichlorodihydrofluorescein diacetate (DCFH-DA) as a fluorescence probe (Fig. 4D). Both PBS group and CSN-IR806/CB group showed negligible green fluorescence of ROS without NIR irradiation whether under normoxia or hypoxia. Under NIR irradiation, the CSN-IR806/CB-treated cells exhibited a significantly strong green fluorescence, suggesting a high concentration of light-induced ROS generation within the cells. Furthermore, it was observed that the fluorescence in CSN-IR806/CB-treated cells under hypoxic conditions was comparatively weaker than that under normoxic conditions on account of the partial limitation on the efficacy of PDT under hypoxia.

To detect the efficient cellular uptake of CSN-IR806/CB, the internalized behavior of CSN-IR806/CB in HepG2 cells under hypoxia was analyzed by using IR806 as the fluorescent indicator through confocal laser scanning microscopy (CLSM) and flow cytometry. The nuclei displayed blue fluorescence after staining with DAPI, whereas the CSN-IR806/CB containing IR806 emitted red fluorescence. As shown in Fig. 4E, there was a gradual increase in the fluorescence intensity of both CSN-IR806/CB and free IR806-treated HepG2 cells over time. Moreover, the fluorescent intensity of CSN-IR806/CB group was significantly higher than that of free IR806 group, contributed to the more effective cellular uptake of CSN-IR806/CB via endocytosis mechanism compared to passive diffusion [40]. Based on the data of flow cytometry, the mean fluorescent intensity of CSN-IR806/CB group was 4.1 times that of free IR806 group at 4 h (Fig. 4F, G), which was consistent with the quantitative analysis by CLSM.

We next investigated whether CSN-IR806/CB could trigger tumor immunogenic cell death (ICD) effects against HepG2 cells by analyzing several typical biomarkers [41, 42]. The three typical characteristics of ICD were the secretion of adenosine triphosphate (ATP) into the extracellular environment, an increased release of high-mobility group box 1 (HMGB1), and a notable surface exposure of calreticulin (CRT) [43]. As shown in Additional file 1: Fig. S11, the CSN-IR806/CB-treated cells under hypoxia with NIR irradiation exhibited the heaviest release of ATP, CRT, and HMGB1. Therefore, the above results demonstrate that CSN-IR806/CB could effectively induce ICD in cancer cells under hypoxia with NIR irradiation.

In vivo pharmacokinetics, biodistribution, and photomediated imaging

Generally, nanomedicine have the potential to improve the effectiveness of antitumor treatments by prolonging the circulation of therapeutic agents in the bloodstream, leading to increased accumulation at tumor sites. To assess whether CSN-IR806/CB possess this characteristic, we conducted a study on the blood circulation profiles of free IR806 and CSN-IR806/CB. As illustrated in Fig. 5A, free IR806 was rapidly cleared from the bloodstream following intravenous administration. In contrast, CSN-IR806/CB presented significantly prolonged blood circulation time, indicating their potential as a candidate for an effective nanomedicine.

Sequentially, the noninvasive near-infrared optical imaging technique was utilized to investigate the biodistribution of free IR806 and CSN-IR806/CB (Fig. 5B) at predetermined time points. The intra-tumoral fluorescence was scarcely observed in the mice intravenously administered with free IR806 throughout the entire experimental period, indicating its rapid clearance in the blood circulation. Nevertheless, the mice intravenously injected with CSN-IR806/CB exhibited a progressive increase in intra-tumoral fluorescence over time, and reached the maximum at 12 h, demonstrating that CSN-IR806/CB significantly boosted the IR806 accumulation in tumors. Ex vivo imaging and semi-quantitative assay of major organs (heart, liver, spleen, lung, and kidney) and the tumor was also performed at 12 and 24 h post-injection of CSN-IR806/CB (Fig. 5C, D). At 0.5 h post-injection, CSN-IR806/CB exhibited a higher IR806 fluorescence at the tumor site and liver compared to other organs. At 24 h post-injection, the IR806 fluorescence was obviously weakened at liver induced by the metabolic and detoxification functions of the liver, and still stronger in the tumor region than in other normal organs, confirming the exceptional tumor enrichment capacity of CSN-IR806/CB [44]. Overall, CSN-IR806/CB has the superior ability to passively target tumor tissue and remain localized at the tumor site.

Based on the results of biodistribution, the tumor regions were subjected to NIR irradiation (808 nm, 1.0 W/cm^2, 5 min) at 12 h after injection, and the hyperthermia study was performed by a thermal imaging camera (Fig. 5E, F). The control group with PBS injection showed negligible temperature increase with 2.2 °C. The CSN-IR806/CB-injected mice exhibited a significantly higher temperature increase (14.5 °C) compared to the IR806-injected ones (5.3 °C), suggesting enhanced accumulation of CSN-IR806/CB at the tumor site. The temperature of 46.1 °C on the tumor surfaces in CSN-IR806/

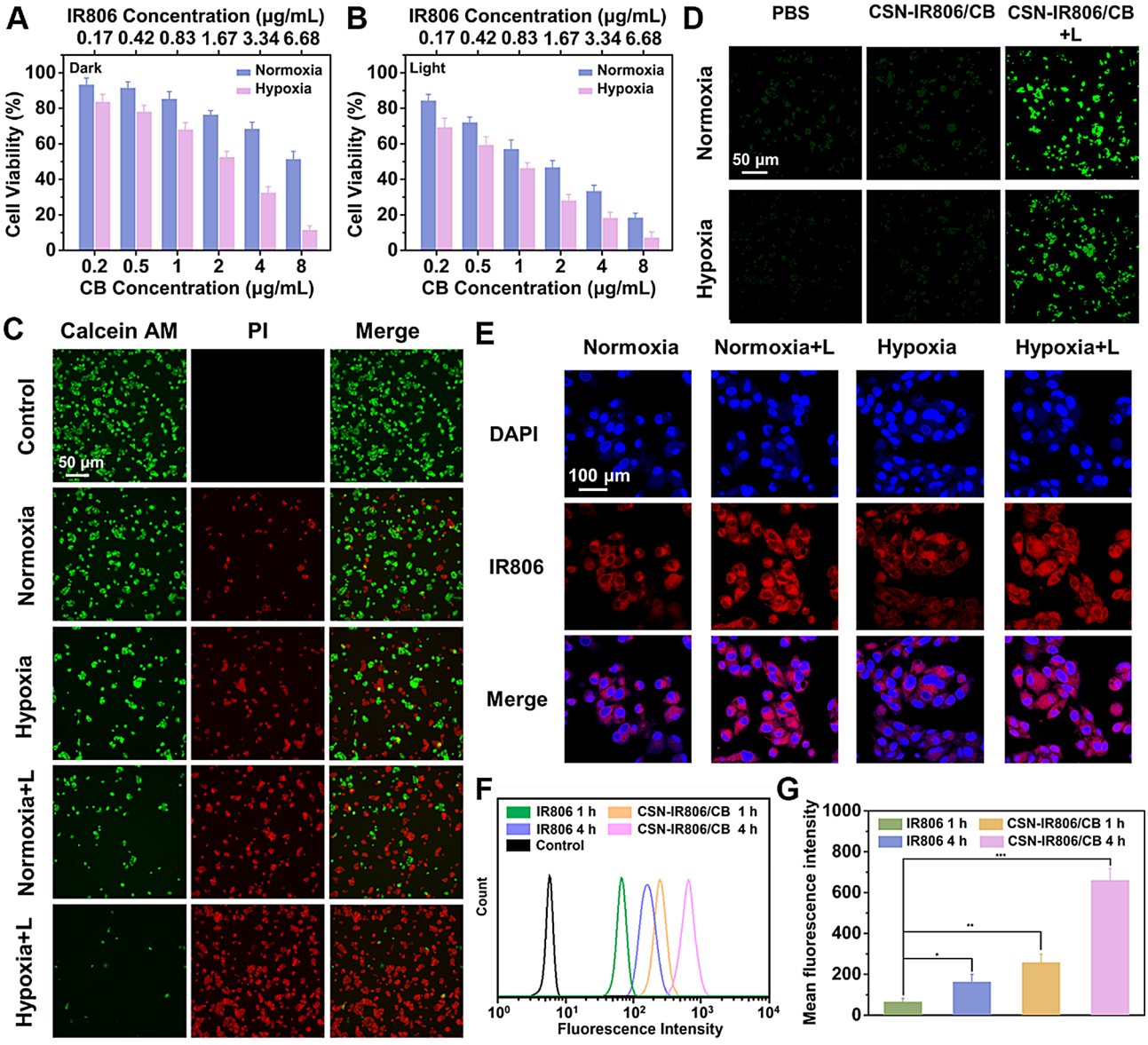

Fig. 4 In vitro cell cytotoxicity of CSN-IR806/CB against HepG2 cells after incubation for 48 h under normoxia or hypoxia (**A**) in the dark or (**B**) under NIR irradiation. (**C**) Live/dead assay of AM/PI co-stained HepG2 cells after various treatments. (**D**) Fluorescence images of ROS level after different treatments using DCFH-DA as ROS fluorescence probe. (**E**) CLSM images of HepG2 cells after incubation with free IR806 or CSN-IR806/CB under hypoxia for 1–4 h. (**F**) Flow cytometric curves of IR806, and (**G**) the corresponding mean fluorescence intensity after incubation with free IR806 or CSN-IR806/CB under hypoxia for 1–4 h

CB group exhibited a mild photothermia effect, which had been demonstrated to effectively treat cancer without causing damage to the skin [45].

In vivo antitumor efficacy and biosafety

The in vivo anticancer efficacy of CSN-IR806/CB combined with NIR irradiation was evaluated by using HepG2 tumor-bearing Balb/c mice as tumor model. PBS, free CB, free IR806, and CSN-IR806/CB were administrated via tail vein injection on day 1 and day 5 (Fig. 6A). As for the light groups, the NIR irradiation (808 nm, 1.0 W/cm^2, 5 min) in tumor regions 12 h post-injection was performed, and then the changes in tumor volume and body weight were monitored every two days. Free CB and free IR806 + L groups both exhibited limited tumor growth inhibition attributed to the rapid clearance of small molecule drugs (Fig. 6B). Without irradiation, CSN-IR806/CB exhibited a moderate therapeutic efficacy, achieving tumor inhibitory rate (TIR) of 59.2% due to the release of some drugs in the hypoxic conditions of the tumor tissues (Fig. 6C). In sharp contrast, CSN-IR806/CB with NIR irradiation significantly reduced tumor volume with the highest TIR of 85.4% due to the synergistic triple therapeutic effect of PTT-PDT-CT.

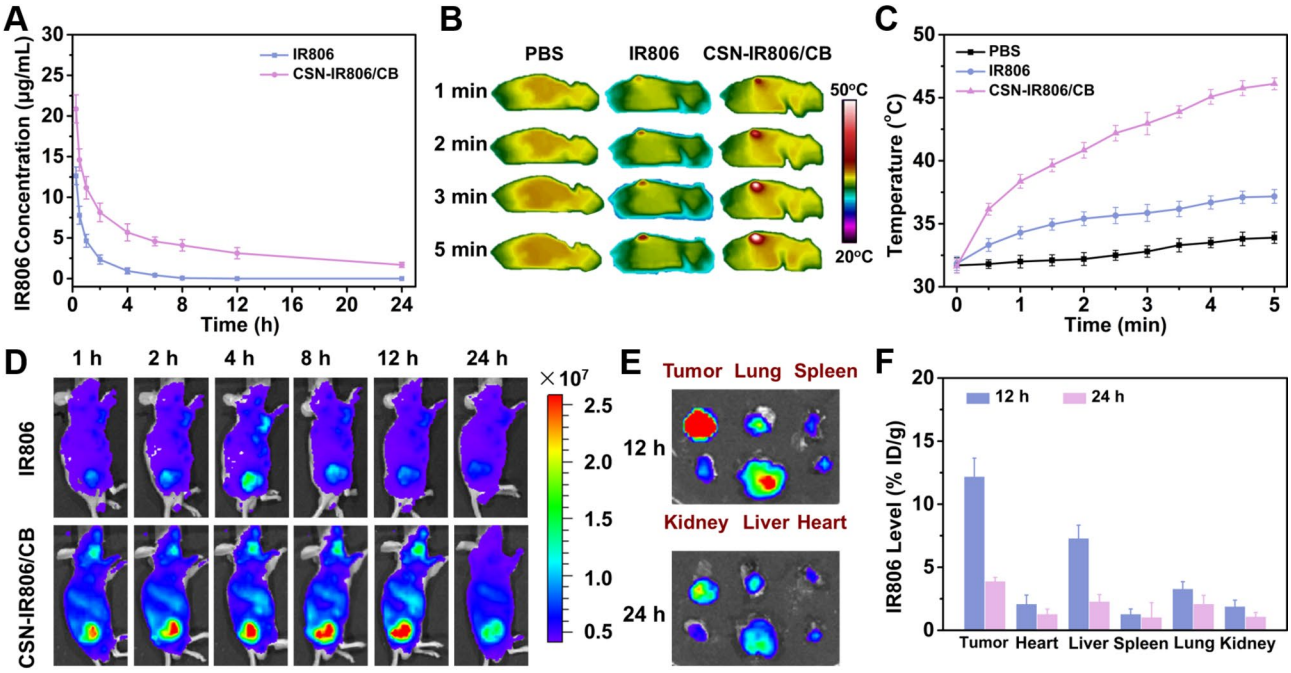

Fig. 5 (**A**) Pharmacokinetics profiles of free IR806 and CSN-IR806/CB. (**B**) In vivo biodistribution of nude mice after intravenous injection of free IR806 and CSN-IR806/CB at different times. (**C**) Ex vivo imaging and (**D**) biodistributions of CSN-IR806/CB group in tumor tissue and major organs at 12 h and 24 h. (**E**) Infrared thermal images and (**F**) time-dependent temperature increase of HepG2 tumor-bearing mice under NIR irradiation at selected time intervals

Furthermore, in vivo biosafety of CSN-IR806/CB was further evaluated. None of the treated groups exhibited significant body weight loss or showed any apparent pathological damage in major organ during the treatment (Fig. 6D, and Additional file 1: Fig. S12), indicating that there was no apparent impairment of organ function throughout the therapy. The above results approved that the CSN-IR806/CB did not elicit any discernible adverse effects in vivo. The H&E staining, TUNEL, and PCNA assays was further used to analyze antitumor effect. (Fig. 6E). The largest area of tumor necrosis, the most cellular apoptosis, and the least cellular proliferation was observed in CSN-IR806/CB + L group, confirmed the most significant tumor-killing ability of PTT-PDT-CT synergistic triple therapies.

Finally, blood samples were obtained from the PBS, CSN-IR806/CB, and CSN-IR806/CB + L groups to assess potential in vivo toxicity through a complete blood count and biochemical analysis. As illustrated in Fig. 7A, parameters such as white blood cells (WBC), red blood cells (RBC), hemoglobin (HGB), hematocrit (HCT), mean corpuscular volume (MCV), mean corpuscular hemoglobin concentration (MCHC), mean corpuscular hemoglobin (MCH), and platelets (PLT) were evaluated for the complete blood count. Concurrently, alanine aminotransferase (ALT), aspartate aminotransferase (AST), total protein (TP), albumin (ALB), alkaline phosphatase (ALP), blood urea nitrogen (BUN), lactate dehydrogenase (LDH), and uric acid levels (UA) were analyzed for biochemical assessment as shown in Fig. 7B. The results indicated that all parameters of the CSN-IR806/CB group both with and without irradiation showed minimal changes compared to the control group. These findings suggest that CSN-IR806/CB may serve as an effective and safe agent for cancer therapy under 808 nm NIR.

Conclusion

In summary, we have successfully prepared a hypoxia-responsive supramolecular nanoprodrug (CSN-IR806/CB) with a cross-linked core, which consist of a dendritic drug-drug conjugates IR806-$(Azo\text{-}CB)_4$ and β-cyclodextrin grafted PEG-D-poly(glutamic acid) block copolymer (PEG-PGlu-CD) via the synergy of π-π stacking interaction, host-guest complexation, hydrogen bonds, and hydrophobic interaction. CSN-IR806/CB exhibited superior physiological stability, effectively preventing the toxicity of free drugs to normal tissues. Both the in vitro and in vivo anti-tumor experimental results that the treatment of IR806-$(Azo\text{-}CB)_4$ with NIR light irradiation presented significantly strong cytotoxicity to HepG2 tumor cells and the TIR of mice reached 85.4% on day 22 resulted from the synergistic triple therapeutic effect of PTT-PDT-CT. Therefore, the IR806-$(Azo\text{-}CB)_4$ provides a charming nanomedicine-based DDSs for combination therapy.

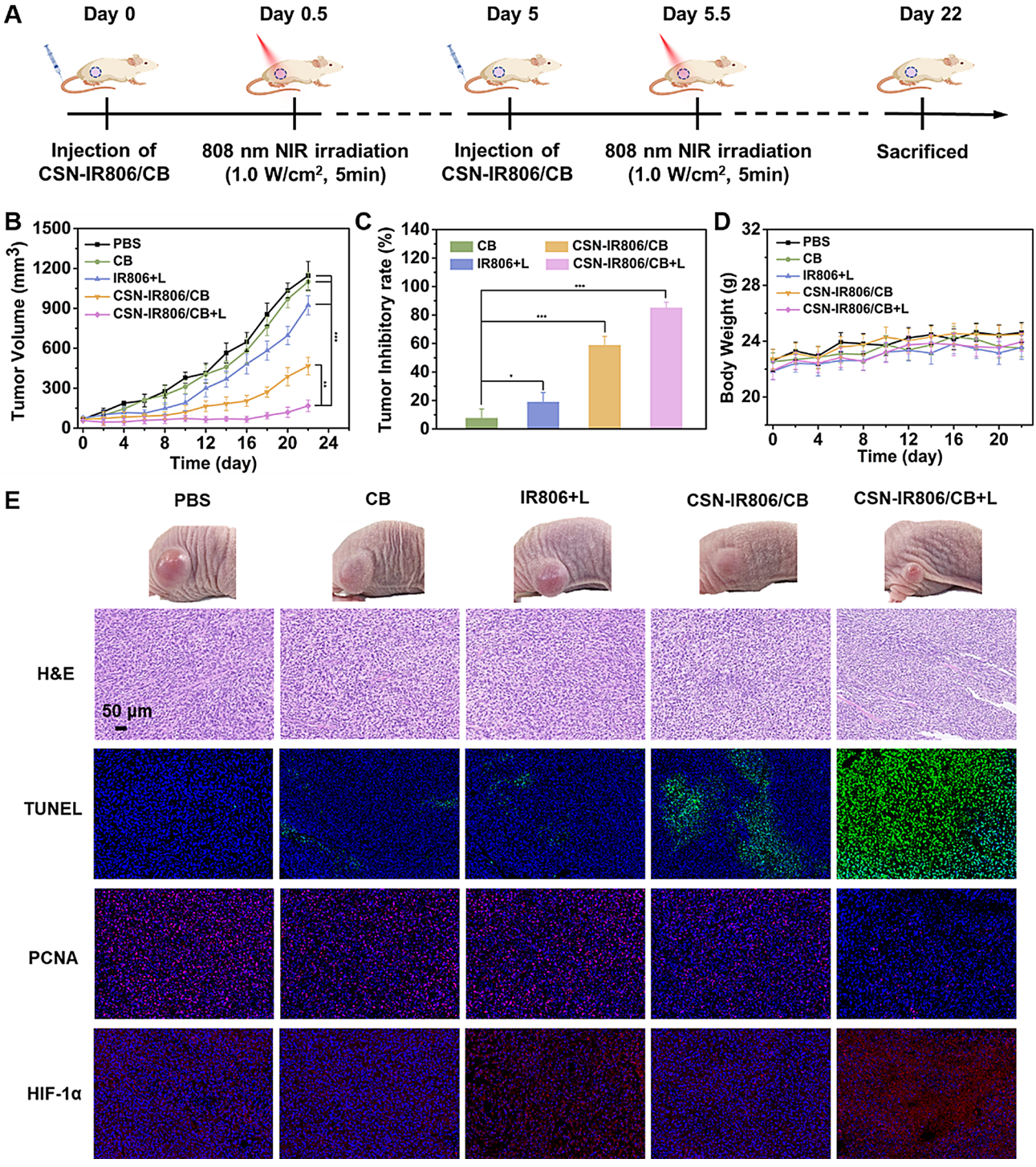

Fig. 6 (**A**) Schematic illustration experiment design for CSN-IR806/CB + L group. (**B**) Time-dependent HepG2 tumor growth curves. (**C**) TIR for different groups. (**D**) Body weight changes of mice on time. (**E**) Photographs of tumors at the end of treatment, and H&E, TUNEL, PCNA, and HIF-1α staining images of tumor tissues at the end of experiment. $^{*}P < 0.1$, and $^{***}P < 0.001$

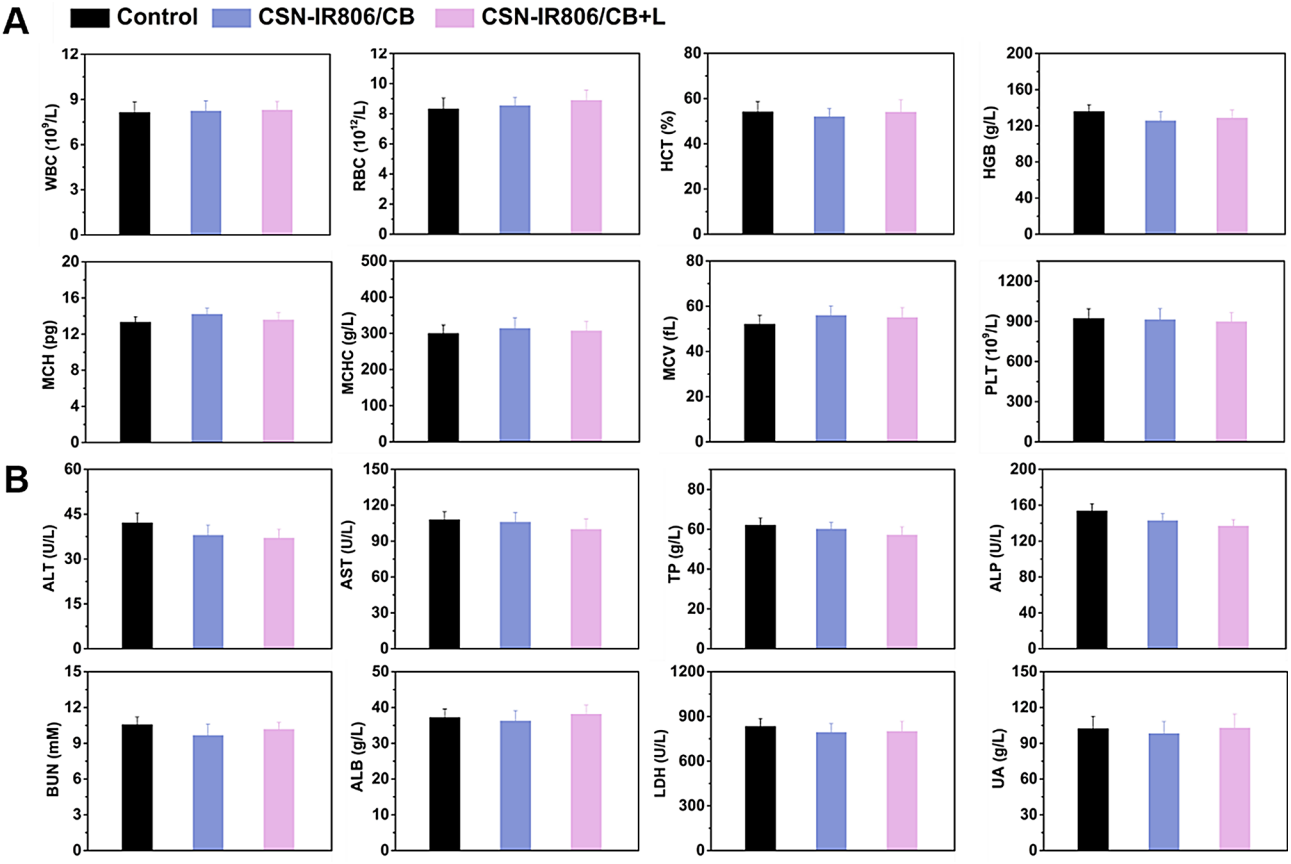

Fig. 7 (**A**) Complete blood panel analysis of mice including WBC, RBC, HCT, HGB, MCH, MCHC, MCV, and PLT. (**B**) Blood biochemistry analysis of mice including ALT, AST, TP, ALP, BUN, ALB, LDH, and UA

Supplementary Information

The online version contains supplementary material available at https://doi.org/10.1186/s12951-025-03394-y.

Supplementary Material 1

graphical abstract

Acknowledgements

This work was financially supported by the Science and Technology Project of Nantong City (MS2023040), the Natural Science Foundation of Jiangsu Province (BK20240950), Innovation Program of Shanghai Municipal Education Commission (20230548), Shanghai Key Laboratory of Cell Engineering (14DZ2272300). The Investigator-initiated Trial Program of Shanghai Pudong New Area Health Commission (the Medical and Industrial Integration Program, 2025-PWYC-04), and Project of Shanghai Municipal Health Commission (202240347).

Author contributions

YD, YX, and CD performed the experiments and wrote the draft manuscript. LZ, ML, TC, and YS analyzed the data and drew the Schemes and Figures. JD polished the English. YD, JD, and BN got the funding and designed the project. All authors read and approved the final manuscript.

Funding

Science and Technology Project of Nantong City, MS2023040, Yue Ding; Natural Science Foundation of Jiangsu Province, BK20240950, Yue Ding; Innovation Program of Shanghai Municipal Education Commission, 20230548, Jin Ding; Shanghai Key Laboratory of Cell Engineering, 14DZ2272300. The Investigator-initiated Trial Program of Shanghai Pudong New Area Health Commission (the Medical and Industrial Integration Program), 2025-PWYC-04, and Project of Shanghai Municipal Health Commission, 202240347, Beifang Ning.

Data availability

No datasets were generated or analysed during the current study.

Declarations

Ethics approval and consent to participate

All animal experiments were approved by the Animal Ethics Committee of Nantong University.

Consent for publication

All authors in the paper agree to be published. The preprint is on https://www.xxx.

Competing interests

The authors declare no competing interests.

Conflict of interest

The authors declare no conflict of interest.

Received: 10 October 2024 / Accepted: 15 April 2025
Published online: 26 April 2025

References

1. Kim Y, Uthaman S, Pillarisetti S, Noh K, Huh KM, Park I-K. Bioactivatable reactive oxygen species-sensitive nanoparticulate system for chemo-photodynamic therapy. Acta Biomater. 2020;108:273–84.

2. Luo L, Xu F, Peng H, Luo Y, Tian X, Battaglia G, Zhang H, Gong Q, Gu Z, Luo K. Stimuli-responsive polymeric prodrug-based nanomedicine delivering Nifuroxazide and doxorubicin against primary breast cancer and pulmonary metastasis. J Control Release. 2020;318:124–35.
3. Torices R, Gómez JM, Pannell JR. Kin discrimination allows plants to modify investment towards pollinator attraction. Nat Commun. 2018;9:2018.
4. Zhang H, Chen W, Wang J, Du W, Wang B, Song L, Hu Y, Ma X. A novel ROS-activable self-immolative prodrug for tumor-specific amplification of oxidative stress and enhancing chemotherapy of Mitoxantrone. Biomaterials. 2023;293:121954.
5. Qin Y, Tong F, Zhang W, Zhou Y, He S, Xie R, Lei T, Wang Y, Peng S, Li Z, Leong J, Gao H, Lu L. Self-delivered supramolecular nanomedicine with transformable shape for ferrocene-amplified photodynamic therapy of breast cancer and bone metastases. Adv Funct Mater. 2021;31:121954.
6. Ding Y, Yu W, Wang J, Ma Y, Wang C, Wang Y, Lu B, Yao Y. Intelligent supramolecular nanoprodrug based on anionic water-soluble [2]biphenyl-extended-pillar[6]arenes for combination therapy. ACS Macro Lett. 2022;11:830–4.
7. Dong X, Brahma RK, Fang C, Yao SQ. Stimulus-responsive self-assembled prodrugs in cancer therapy. Chem Sci. 2022;13:4239–69.
8. Qu H, Li L, Chen H, Tang M, Cheng W, Lin TY, Li L, Li B, Xue X. Drug-drug conjugates self-assembled nanomedicines triggered photo-/immuno- therapy for synergistic cancer treatments. J Control Release. 2023;363:361–75.
9. Deng Z, Liu S. Controlled drug delivery with nanoassemblies of redox-responsive prodrug and polyprodrug amphiphiles. J Controlled Release. 2020;326:276–96.
10. Huang L, Zhao S, Fang F, Xu T, Lan M, Zhang J. Advances and perspectives in carrier-free nanodrugs for cancer chemo-monotherapy and combination therapy. Biomaterials. 2020;268:120557.
11. Zhou S, Hu X, Xia R, Liu S, Pei Q, Chen G, Xie Z, Jing X. A Paclitaxel prodrug activatable by irradiation in a hypoxic microenvironment. Angew Chem Int Edit. 2020;59:23198–205.
12. Fan Z, Wang Y, Xiang S, Zuo W, Huang D, Jiang B, Sun H, Yin W, Xie L, Hou Z. Dual-self-recognizing, stimulus-responsive and carrier-free methotrexate–mannose conjugate nanoparticles with highly synergistic chemotherapeutic effects. J Mater Chem B. 2020;8:1922–34.
13. Zhou Z, Cong M, Li M, Tintaru A, Li J, Yao J, Xia Y, Peng L. Negative dendritic effect on enzymatic hydrolysis of dendrimer conjugates. Chem Commun. 2018;54:5956–9.
14. Li Y, Li Y, Zhang X, Xu X, Zhang Z, Hu C, He Y, Gu Z. Supramolecular pegylated dendritic systems as pH/redox dual-responsive theranostic nanoplatforms for platinum drug delivery and NIR imaging. Theranostics. 2016;6:1293.
15. Duncan R, Izzo L. Dendrimer biocompatibility and toxicity. Adv Drug Deliver Rev. 2005;57:2215–37.
16. Geng W-C, Sessler JL, Guo D-S. Supramolecular prodrugs based on host–guest interactions. Chem Soc Rev. 2020;49:2303–15.
17. Yu G, Jie K, Huang F. Supramolecular amphiphiles based on host–guest molecular recognition motifs. Chem Rev. 2015;115:7240–303.
18. Zhou J, Rao L, Yu G, Cook TR, Chen X, Huang F. Supramolecular cancer nanotheranostics. Chem Soc Rev. 2021;50:2839–91.
19. Zhou J, Yu G, Huang F. Supramolecular chemotherapy based on host–guest molecular recognition: a novel strategy in the battle against cancer with a bright future. Chem Soc Rev. 2017;46:7021–53.
20. George Joy J, Sharma G, Kim J-C. Tailoring polymeric nanocarriers for hypoxia-specific drug release: insights into design and applications in clinics. Chem Eng J. 2024;496:153978.
21. He X, Wang J, Liu X, Niu Q, Li Z, Chen B, Xiong Q. Hypoxia-responsive hydrogen-bonded organic framework-mediated protein delivery for cancer therapy. Adv Healthc Mater. 2024; 2400747.
22. Li M, Dong Y, Wang Z, Zhao Y, Dai Y, Zhang B. Engineering hypoxia-responsive 6-aminonicotinamide prodrugs for on-demand NADPH depletion and redox manipulation. J Mater Chem B. 2024;12:8067–75.
23. Ding Y, Yu W, Shen R, Zheng X, Zheng H, Yao Y, Zhang Y, Du C, Yi H. Hypoxia-responsive tetrameric supramolecular polypeptide nanoprodrugs for combination therapy. Adv Healthc Mater. 2024;13:2303308.
24. Kang Y, Lim J, Saravanakumar G, Kim J, Park M, Im S, Kim WJ. Immunostimulation of tumor microenvironment by targeting tumor-associated macrophages with hypoxia-responsive nanocomplex for enhanced anti-tumor therapy. J Control Release. 2022;343:78–88.
25. Kumari R, Sunil D, Ningthoujam RS. Hypoxia-responsive nanoparticle based drug delivery systems in cancer therapy: an up-to-date review. J Control Release. 2020;319:135–56.
26. Li Y, Jeon J, Park JH. Hypoxia-responsive nanoparticles for tumor-targeted drug delivery. Cancer Lett. 2020;490:31–43.
27. Yang G, Phua SZF, Lim WQ, Zhang R, Feng L, Liu G, Wu H, Bindra AK, Jana D, Liu Z. A hypoxia-responsive albumin-based nanosystem for deep tumor penetration and excellent therapeutic efficacy. Adv Mater. 2019;31:1901513.
28. Zhang TX, Zhang ZZ, Yue YX, Hu XY, Huang F, Shi L, Liu Y, Guo DS. A general hypoxia-responsive molecular container for tumor-targeted therapy. Adv Mater. 2020;32:1908435.
29. Ding Y, Wang C, Ma Y, Zhu L, Lu B, Wang Y, Wang J, Chen T, Dong C-M, Yao Y. pH/ROS dual-responsive supramolecular polypeptide prodrug nanomedicine based on host-guest recognition for cancer therapy. Acta Biomater. 2022;143:381–91.
30. Xu H, Han Y, Zhao G, Zhang L, Zhao Z, Wang Z, Zhao L, Hua L, Naveena K, Lu J, Yu R, Liu H. Hypoxia-responsive lipid–polymer nanoparticle-combined imaging-guided surgery and multitherapy strategies for glioma. Acs Appl Mater Inter. 2020;12:52319–28.
31. Li H, Zhang X, Chen S, Cao C, Zhang X, Li X, Xing S, Jia S, Li J, Wang S. Hypoxia exacerbation-triggered doxorubicin prodrug activation for sequential photodynamic/chemotherapy. Acs Mater Lett. 2024;6:2599–608.
32. Yu G, Zhao X, Zhou J, Mao Z, Huang X, Wang Z, Hua B, Liu Y, Zhang F, He Z. Supramolecular polymer-based nanomedicine: high therapeutic performance and negligible long-term immunotoxicity. J Am Chem Soc. 2018;140:8005–19.
33. Zheng X, Pan D, Chen X, Wu L, Chen M, Wang W, Zhang H, Gong Q, Gu Z, Luo K. Self-stabilized supramolecular assemblies constructed from pegylated dendritic peptide conjugate for augmenting tumor retention and therapy. Adv Sci. 2021;8:2102741.
34. Sun L, Zhao P, Chen M, Leng J, Luan Y, Du B, Yang J, Yang Y, Rong R. Taxanes prodrug-based nanomedicines for cancer therapy. J Control Release. 2022;348:672–91.
35. Li Y, Lin J, Wang P, Luo Q, Lin H, Zhang Y, Hou Z, Liu J, Liu X. Tumor microenvironment responsive shape-reversal self-targeting virus-inspired nanodrug for imaging-guided near-infrared-II photothermal chemotherapy. ACS Nano. 2019;13:12912–28.
36. Yang Z, Luo Y, Hu Y, Liang K, He G, Chen Q, Wang Q, Chen H. Photothermo-promoted nanocatalysis combined with H2S-mediated respiration Inhibition for efficient cancer therapy. Adv Funct Mater. 2021;31:2007991.
37. Tang Y, Wang X, Zhu G, Liu Z, Chen XM, Bisoyi HK, Chen X, Chen X, Xu Y, Li J. Hypoxia-responsive photosensitizer targeting dual organelles for photodynamic therapy of tumors. Small. 2023;19:2205440.
38. Xie Q, Liu Y, Long Y, Wang Z, Jiang S, Ahmed R, Daniyal M, Li B, Liu B, Wang W. Hybrid-cell membrane-coated nanocomplex-loaded Chikusetsusaponin IVa Methyl ester for a combinational therapy against breast cancer assisted by Ce6. Biomater Sci. 2021;9:2991–3004.
39. Yu J, Zhang B, Li J, Wang Z, Xu Z, Wang Y, Zhou T, Huang R, Ye J, Zhang H. Transforming enemy into friend strategy-based stimuli responsive dual-drug liposomes for synergistic chemo-photodynamic therapy. Chem Eng J. 2024;487:150526.
40. Ao M, Yu F, Li Y, Zhong M, Tang Y, Yang H, Wu X, Zhuang Y, Wang H, Sun X. Carrier-free nanoparticles of camptothecin prodrug for chemo-photothermal therapy: the making, in vitro and in vivo testing. J Nanobiotechnol. 2021;19:1–15.
41. He M, Song Y, Xu W, Zhang X, Dong C. Four birds with one stone: A multifunctional polypeptide nanocomposite to unify ferroptosis, nitric oxide, and photothermia for amplifying antitumor immunity. Adv Funct Mater. 2023;33:2304216.
42. Liu X, Wang H, Li Z, Li J, He S, Hu C, Song Y, Gao H, Qin Y. Transformable self-delivered supramolecular nanomaterials combined with anti-PD-1 antibodies alleviate tumor immunosuppression to treat breast cancer with bone metastasis. J Nanobiotechnol. 2024;22:566.
43. Zhong D, Hou X, Pan D, Li Z, Gong Q, Luo K. Bioorthogonal in situ polymerization of dendritic agents for hijacking lysosomes and enhancing antigen presentation in cancer cells. Adv Mater. 2024;36:2403588.

44. Gong L, Zhang Y, Zhao J, Zhang Y, Tu K, Jiao L, Xu Q, Zhang M, Han S. All-in-one biomimetic nanoplatform based on Hollow polydopamine nanoparticles for synergistically enhanced radiotherapy of colon cancer. Small. 2022;18:2107656.
45. Melamed JR, Edelstein RS, Day ES. Elucidating the fundamental mechanisms of cell death triggered by photothermal therapy. ACS Nano. 2015;9:6–11.

Publisher's note